Flow-Field Dynamics of a Flexible Flapping Airfoil using a Navier-Stokes Solver

Salil Harris ¹ and Sunetra Sarkar ¹ * ¹Indian Institute of Technology Madras Chennai - 600 036, Tamil Nadu, India

Abstract

Nature's flyers have been an inspiration in the development of flapping wing MAVs. The secret to their flight has been attributed to the wing kinematics and wake patterns generated. The wing kinematics used in flapping wing studies is usually sinusoidal. But in reality, a flexible flight motor dictates the kinematics. In the current work, a Duffing oscillator model of the insect flight motor is used to predict the kinematics, in the presence wing loads that are computed by a two-dimensional Navier-Stokes solver. This fluid-structure interaction problem uses a discrete vortex method solver to solve for the fluid part and a Runge-Kutta solver to solve for the structural part. The present work investigates the structural response exhibited by the flexible insect flight-motor, and the corresponding wake structures and loads in a sub-resonance regime. A period-doubling route to chaotic structural response is identified, which is reflected in the flow-field and the aero-dynamic loads.

Keyword: Flapping wings, Discrete vortex method, Fluid-Structure Interaction

1 Introduction

Development of Micro Aerial Vehicles (MAVs) with capabilities exceeding that of a conventional aircraft have attracted a lot of attention in recent years. The interest in biologically-inspired propulsion mechanisms have peaked as insects and birds, with their amazing range of maneuvers and

^{*}Corresponding author e-mail: sunetra.sarkar@gmail.com

efficient flight, form an inspiration in the development of MAVs with flapping wings.

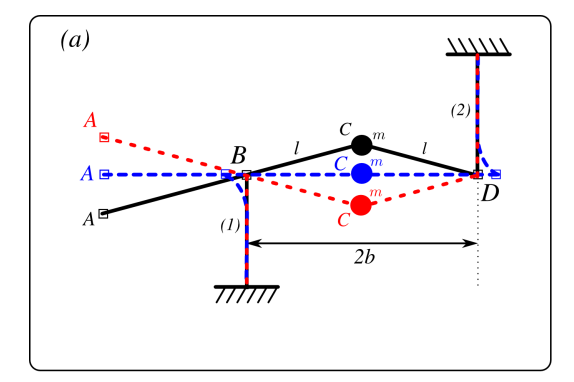
The efficient flight of insects has been attributed to the flapping motion (kinematics) of their wings and the corresponding wake structures downstream of the wings [17]. The problem of flapping wings poses a challenge for conventional CFD methods, as it is inherently a moving body problem. Different computational techniques used in flapping wing problems include immersed boundary method [20], vortex methods [19], arbitrary Lagrangian-Eulerian (ALE) methods [8] etc.

In a two-dimensional framework, usually the insect wing is approximated as an airfoil, and its flapping motion is modeled using two fundamental kinematics – plunge (translational) and pitch (rotational). The forces produced on a flapping wing are strongly dependent on the wake structures in its downstream [17]. The wake structures and mean thrust produced by a sinusoidally plunging airfoil has been experimentally investigated by Lai & Platzer [16]. Koochesfahani [11] has experimentally investigated the wake structures downstream of a pitching airfoil and Mackowski et al. [12] have measured the thrust produced by it. A combination of plunge and pitch kinematics was also investigated experimentally by Anderson et al. [1], and it was found that conditions of high propulsive efficiency are obtained when the pitching and plunging motions have a phase difference of 90°. Furthermore, comparison of periodic non-sinusoidal plunge kinematics with sinusoidal ones has also been reported in Sarkar et al. [19].

However, in all these works, the flapping foil is assumed to be a rigid body harmonically oscillating in a flowing fluid. In reality, the insect wing is a flapping body whose kinematics is governed by an in-built flexible flightmotor. Brennan et al. [4] have modeled the flexible insect flight-motor as a forced-damped Duffing oscillator. The linear viscous damper in their oscillator represents the damping forces acting on the insect wing (lift and thrust), and the external forcing represents the control loads from the insect muscles to the flight-motor. The present work, however, improves this model by computing the aerodynamic loads using an unsteady Navier-Stokes solver, which essentially results in a Fluid-Structure Interaction (FSI) problem.

1.1 The simplified flight motor

Brennan et al. [4] modeled the insect flight-motor as a linkage system ABCD shown in Figure 1a with columns (1) and (2) attached to joints B and D respectively, and the entire mass of the system concentrated at C. The mass m at C, under the influence of a non-dimensional forcing $\Gamma \sin(\omega t)$, oscillates in



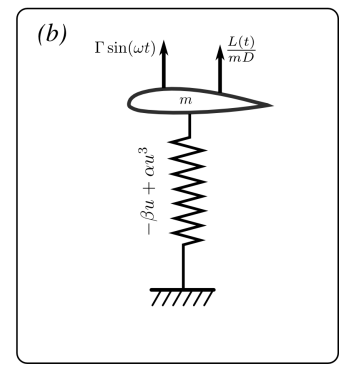


Figure 1: Linkage mechanism of insect-flight-motor modeled by Brennan et al. [4] as a forced Duffing-type oscillator

a plunge degree-of-freedom. This oscillation of C causes bending of columns (1) and (2) (Figure 1a). This bending of columns essentially represents the stiffness of the insect flight-motor. This has been modeled by Brennan et al. [4] as a spring with a linear and non-linear stiffness (Figure 1b). The concentrated mass m at C is assumed to be a two-dimensional section of the insect wing (airfoil), in the current work, as shown in Figure 1b. The plunge-type motion of this airfoil is dictated by the non-dimensional forcing $\Gamma \sin(\omega t)$, in the presence of a spring (with linear and non-linear stiffness) and the aerodynamic loads that are obtained from an unsteady Navier-Stokes solver. Furthermore, as the airfoil undergoes only plunge type of motion, lift is the only aerodynamic force to dampen the structural oscillations.

This essentially results in an undamped forced Duffing-type oscillator, with a lift force L(t) as shown in Eqn. 1. The non-dimensionalization is in accordance with [4]

$$\ddot{u} - \beta u + \alpha u^3 = \Gamma \sin(\omega t) + \frac{L(t)}{mD} \tag{1}$$

where u is a non-dimensional displacement normalized with a characteristic length $D=\sqrt{\frac{2(1-\frac{b}{l})}{\frac{b}{l^3}}}$, (°) is the second derivative with respect to time, $\alpha=\beta=\frac{\omega_0^2}{2}$ where β and α are linear and non-linear non-dimensional stiffness parameters respectively, $\Gamma=\frac{P}{mD}$ is the non-dimensional forcing parameter, P is the forcing, $\omega_0^2=\frac{4K}{m}\left(1-\frac{b}{l}\right)$ is the structural natural

frequency, ω is the forcing frequency, K is the stiffness of columns (1) and (2); b and l are lengths of linkage mechanism of the insect flight motor as shown in Figure 1a; the ratio of $\frac{b}{l}$ is maintained at 0.9 throughout this work in accordance with [4].

2 Numerical Methodology

The current work employs a partitioned loosely-coupled [5] FSI solver. This section includes the description of the computational methodology employed in this work, and its validation. The loosely-coupled [5] FSI solver has the aerodynamic part modeled by a Navier-Stokes solver using a particle based Discrete Vortex Method (DVM) [18], and the structural displacements and velocities computed using a fifth order embedded Runge-Kutta (RK) solver [14].

DVM follows a vorticity-velocity formulation of the two-dimensional incompressible Navier-Stokes equations. The results generated by DVM is ensured to be accurate by validating it qualitatively with results of Lai & Platzer [16] and quantitatively with that of Young [21], for the range of parameters chosen for this work. The structural solver is a fifth-order RK solver [14] that ensures time-stepping convergence by comparison of results with a fourth-order RK solver embedded in it. Furthermore, an adaptive time-stepping procedure is employed for faster convergence.

2.1 Discrete Vortex Method

The equations governing the incompressible fluid-flow are given by Navier-Stokes equations [2] shown in Eqns. 2.

$$\nabla \cdot \vec{V} = 0$$
 (Continuity Equation) (2a)

$$\frac{D\vec{V}}{Dt} = -\frac{\nabla p}{\rho} + \nu \nabla^2 \vec{V} \qquad (Momentum Transport) \qquad (2b)$$

Here, $\frac{D}{Dt}$ is the material derivative, ν is the kinematic viscosity, ρ is the density, p is the pressure and \vec{V} is the velocity of the fluid at any point in the domain. This can be written in two-dimensional vorticity transport form [2] as shown in Eqn. 3b. The current problem domain has a body moving in a fluid with no bounds, which has some initial vorticity (Eqn. 3d). The fluid-flow far away from the body remains undisturbed (Eqn. 3e), and

the no-penetration (Eqn. 3f) and no-slip (Eqn. 3g) boundary conditions need to be ensured on the surfaces of the body.

$$\nabla \cdot \vec{V} = 0 \qquad \text{(Continuity Equation)} \tag{3a}$$

$$\frac{D\Omega}{Dt} = \nu \nabla^2 \Omega \qquad \qquad \text{(Vorticity Transport)} \tag{3b}$$

$$\vec{\Omega} = \nabla \times \vec{V} \tag{Vorticity}$$

$$\omega(\vec{x},0) = \omega_0(\vec{x})$$
 (Initial condition) (3d)

$$\vec{V}(\vec{x} \to \infty, t) = \vec{V}_{\infty}$$
 (Infinity BC)

$$\vec{V}(\vec{x}_B, t) \cdot \hat{e}_n = \vec{V}_B \cdot \hat{e}_n$$
 (No-penetration BC)

$$\vec{V}(\vec{x}_B, t) \cdot \hat{e}_s = \vec{V}_B \cdot \hat{e}_s$$
 (No-slip BC)

In the above Eqns. 3, \hat{e}_s and \hat{e}_n are the unit vectors in the tangential and normal directions respectively on the body surface, \vec{V}_B is the velocity of the body, \vec{V}_{∞} is the incoming free-stream velocity and \vec{x} is the position vector.

In the context of vortex methods, vorticity field is discretized into N vortex particles (Eqn. 4).

$$\Omega(\vec{x}) = \sum_{j=1}^{N} \gamma_j f_{\delta}(\vec{x} - \vec{x}_j)$$
(4)

Here, \vec{x}_j are the locations of N vortex particles with circulations γ_j respectively; f_{δ} is a function that defines the vorticity distribution of individual vortex particles. The vorticity transport equation (Eqn. 3b) is split into advection (Eqn. 5a) and diffusion (Eqn. 5b) parts by the method of viscous splitting [3]. The generalized solution procedure in vortex methods is to update the location of the vortex particles in the domain by advecting and diffusing them according to the solutions of Eqns. 5a and 5b respectively, to advance in time.

$$\frac{\partial \Omega}{\partial t} + \vec{V} \cdot \nabla \Omega = 0 \qquad \text{Advection Equation} \qquad (5a)$$

$$\frac{\partial \Omega}{\partial t} = \nu \nabla^2 \Omega \qquad \qquad \text{Diffusion Equation} \qquad (5b)$$

In vortex methods, the simulation begins by satisfying the no-penetration boundary condition (Eqn. 3f) on the body surface S. For this purpose, a body-bound vortex street whose vortex strength distribution is unknown, is assumed. Then, this vortex sheet is discretized into panels of equal length, and the no-penetration boundary condition is enforced at control points

(mid-points of the panels in this scenario) to obtain the strength distribution of the vortex sheet. However, this method of enforcing the no-penetration boundary condition (Eqn. 3f) will, in general, violate the no-slip boundary condition (Eqn. 3g).

The non-zero slip-velocity predicted by the aforementioned panel method is cancelled out by generating new vortex particles that are placed at some finite distance above the control points. Once the no-penetration (Eqn. 3f) and no-slip (Eqn. 3g) boundary conditions are satisfied and new vortex particles are generated, the velocity required to advect these vortex particles is calculated.

The advection equation (Eqn. 5a) implies that the vorticity remains constant along a fluid path. Hence, a vortex particle can be advected from one location to another without change in its strength [15], provided the velocity field is known.

From the definition of vorticity (Eqn. 3c) and the requirement of an incompressible (Eqn. 2a) velocity field, a Poisson's equation (Eqn. 6) relating the streamfunction ψ to vorticity can be obtained [15].

$$\nabla^2 \psi = -\Omega \tag{6}$$

The solution to ψ in Eqn. 6 is obtained using the Green's function method, and its derivative as shown in Eqn. 7 gives the velocity to advect the vorticity field.

$$\vec{V} = \left(\frac{\partial}{\partial y}, -\frac{\partial}{\partial x}\right)\psi\tag{7}$$

This procedure results in a vorticity-velocity relationship, the Biot-Savart's law (Eqn. 8), which gives the velocity to advect the vortex particles in the presence of body moving in a flowing fluid [15], [2].

$$\vec{V}(\vec{x}, t) = -\frac{1}{2\pi} \left[\int_{R} \frac{\vec{\Omega} \times (\vec{x}' - \vec{x})}{|\vec{x}' - \vec{x}|^{2}} dR + 2 \int_{S} \frac{\vec{\Omega}_{b} \times (\vec{x}_{B} - \vec{x})}{|\vec{x}_{B} - \vec{x}|^{2}} dS + \vec{V}_{\infty} \right]$$
(8)

Here, R is the fluid region and S is the curve representing the body shape. The first component in the RHS of Eqn. 8 is the velocity induced by a vortex particle with vorticity $\vec{\Omega}$ at \vec{x}' on another vortex particle at \vec{x} . The second component is the velocity induced by the rigid body rotation of the body $(\vec{\Omega}_b)$; here \vec{x}_B is a reference point in the body. The third component is the contribution due to the incoming free-stream velocity.

Furthermore, it is understood from the denominator of the first and second terms in the RHS of Eqn. 8 that the infinity BC (Eqn. 3e) is automatically satisfied. Moreover, it shows that the velocity induced by a particle on

itself is singular. This issue is tackled by usage of vortex blob model [7] that smoothens out the singularity within a cut-off radius (σ) using a smoothing function f_{δ} (Eqn. 4) [15]; the present solver employs a Chorin blob [7]. It should also be noted that in the present solver, the vortex blobs generated to satisfy the no-slip boundary condition (Eqn. 3g) are placed at a distance of σ above the control points such that the tangential (slip) velocity predicted by the application of panel methods is exactly cancelled out.

The diffusion equation (Eqn. 5b) is solved by the method of random walks [7]. The solution to the diffusion equation (Eqn. 5b) is similar to the probability density function of a Gaussian random variable with zero mean and variance of $2\nu t$ [7]. Hence, for a discretized vorticity field, diffusion can be simulated by giving random displacements with zero mean and variance of $2\nu\Delta t$ to the vortex blobs in two orthogonal directions over a discrete time interval of Δt [15].

Once the vortex blobs are advected and diffused, the forces acting on the body are computed. The force computations are done using the theory of vortex momentum [2], wherein the net force \vec{F} on the body is given by the rate of change of vortex momentum \vec{I} as shown in Eqns. 9a and 9b.

$$\vec{I} = (I_x, I_y) = \int_R \vec{x} \times \vec{\Omega} dR$$
 (9a)

$$\vec{F} = -\frac{d\vec{I}}{dt} \tag{9b}$$

A disadvantage of the vortex methods is that they become very slow as time progresses, due to addition of vortex blobs at every time-step. In the present solver, the number of blobs are reduced by the process of blob "annihilation" [15]. Vortex blobs of similar strengths and opposite signs that are very close to each other have insignificant contribution [15] and are hence "annihilated". The method of blob "annihilation" has reduced the number of vortex blobs in the domain to a great extent in the present solver and has been very effective in reducing its aforementioned gradual sluggishness.

2.2 Validation of DVM solver

In the present work, a NACA 0012 airfoil moving in a plunging degree of freedom is chosen as the body. Validation of the fluid solver for a harmonically oscillating airfoil has been done qualitatively by comparing with experimental results of Lai & Platzer [16] and quantitatively by comparing with the Navier-Stokes solutions of Young [21]. Flapping wing MAVs operate at Re = 10000 - 40000 [13] and hence Re = 10000 is maintained throughout

this work. Moreover, the effects of varying Re in these ranges are minimal on loads [10], as they are dictated by trailing wakes that are unaltered at these ranges of Re [9].

For a sinusoidally plunging airfoil, the wake structures and mean-thrust generated have a strong dependence on the non-dimensional plunge velocity $kh_m = \frac{2\pi fh}{V_{\infty}}$ [16]; f is the flapping frequency and h is the plunge amplitude.

According to Young [21], the reduced frequency $k_m = \frac{2\pi fc}{V_{\infty}}$ is also an important parameter in the context of plunging airfoils. The variation in wake structures with kh_m [16] have been used for qualitative comparison. The variation of mean thrust coefficient $C_{T\ mean} = \frac{1}{T} \int_0^T C_T(t) \ dt$ and the peak lift coefficient $C_{L\ peak}$ [21] have been used for quantitative validation; T is the time-period and $C_T(t)$ is the instantaneous thrust coefficient.

Figure 2 shows the wake structures as a function of kh_m and also compares the experimentally generated vorticity plots of Lai & Platzer [16] with wake patterns generated by DVM. At low values of $kh_m = 0.196$, two similar-signed vortices (SSV) are produced in a half-cycle (Figure 2). As kh_m is increased to 0.393, reverse-Kármán type of vortex streets are observed (Figure 2). This reverse-Kármán type of vortex street is maintained till kh_m reaches 1.0 ($kh_m = 0.589$ and 0.786 in Figure 2). Further increase in kh_m results in wake structures deflected from their horizontal alignment ($kh_m = 1.570$ in Figure 2). It can also be seen from Figure 2 that the qualitative results predicted by DVM show a very good match with the experimental vorticity plots of Lai & Platzer [16].

Figure 3 shows the variation of $C_{T\ mean}$ and $C_{L\ peak}$ with kh_m , at $k_m=2.0$, 10.0 and 20.0, compared with that of Young [21]. Both $C_{T\ mean}$ and $C_{L\ peak}$ increase with increase in kh_m , and show a very good match with the values generated by Navier-Stokes solver of Young [21]. The slope of $C_{L\ peak}$ - kh_m curve increases with increase in k_m (Figure 3). However, the slope of $C_{T\ mean}$ - kh_m curve is almost the same between $k_m=10$ and 20, and much higher compared to that of $k_m=2$. This implies that beyond a certain value, an increase of k_m cannot cause a change in $C_{T\ mean}$. However, increase in kh_m causes a significant increase in $C_{L\ peak}$ and $C_{T\ mean}$ values, except at lower values of k_m .

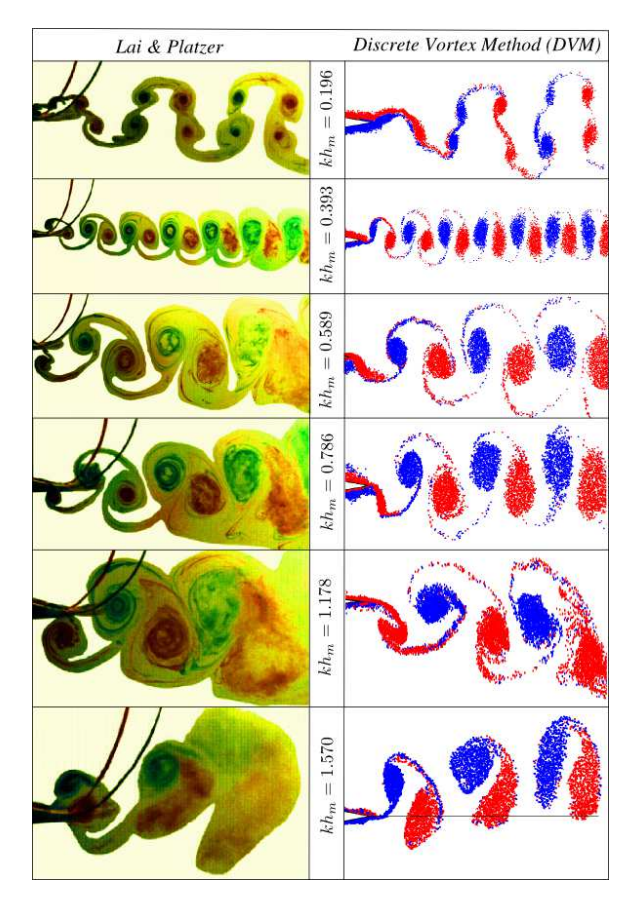


Figure 2: Wake structures generated by DVM, compared with Lai & Platzer [16] at different kh_m

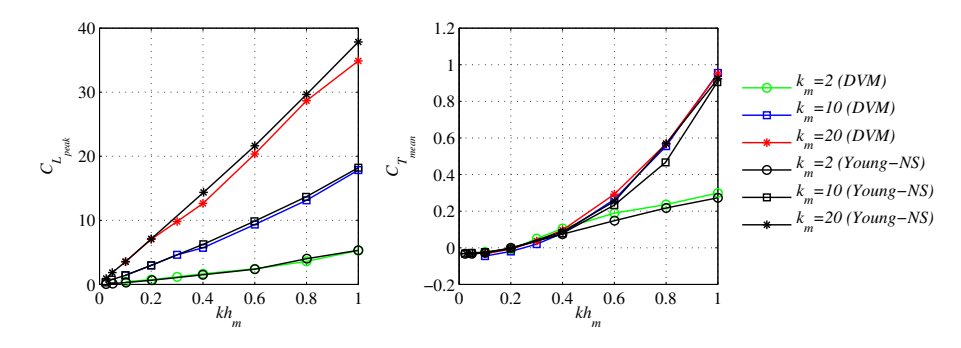


Figure 3: Comparison of $C_{L\ peak}$ and $C_{T\ mean}$ generated by DVM, with Young [21]

2.3 Runge-Kutta solver

The structural equation is a forced Duffing equation given by Eqn. 1, which is an ordinary differential equation that does not have an exact solution and hence is to be solved numerically; the current work uses a Runge-Kutta (RK) solver. Step-sizing is an integral part of RK solvers which essentially dictates its accuracy [14]. Among the many methods proposed for step-sizing convergence of RK solvers, Press et al. [14] have suggested the use of embedded RK solvers, where the step-sizing convergence is dictated by comparing the results predicted by the two RK solvers embedded in it. The current work uses a fifth-order RK solver which has a fourth-order RK solver embedded in it [14]. Here, the step-sizing convergence is decided by comparing the result of fifth-order RK solver with the embedded fourth-order RK solver [14], and if the error is within the tolerance limit, the value generated by the fifth-order solver is chosen [14] such that the solver remains accurate to the fifth-order. Moreover, an adaptive step-sizing is employed for faster convergence.

The equation for the fifth-order scheme is given by

$$u_{n+1} = u_n + c_1 r_1 + c_2 r_2 + c_3 r_3 + c_4 r_4 + c_5 r_5 + c_6 r_6 + O(h^6)$$
 (10)

and the embedded fourth-order embedded scheme is given by

$$u_{n+1}^* = u_n + c_1^* r_1 + c_2^* r_2 + c_3^* r_3 + c_4^* r_4 + c_5^* r_5 + c_6^* r_6 + O(h^5)$$
(11)

where

$$r_{1} = \Delta t \ f(t_{n}, u_{n})$$

$$r_{2} = \Delta t \ f(t_{n} + a_{2}h, u_{n} + b_{21}r_{1})$$

$$r_{3} = \Delta t \ f(t_{n} + a_{3}h, u_{n} + b_{31}r_{1} + b_{32}r_{2})$$

$$r_{4} = \Delta t \ f(t_{n} + a_{4}h, u_{n} + b_{41}r_{1} + b_{42}r_{2} + b_{43}r_{3})$$

$$r_{5} = \Delta t \ f(t_{n} + a_{5}h, u_{n} + b_{51}r_{1} + b_{52}r_{2} + b_{53}r_{3} + b_{54}r_{4})$$

$$r_{6} = \Delta t \ f(t_{n} + a_{6}h, u_{n} + b_{61}r_{1} + b_{62}r_{2} + b_{63}r_{3} + b_{64}r_{4} + b_{65}r_{5})$$

where u_n and u_{n+1} are values at n-th and (n+1)-th steps, Δt is the step-size, r_i 's are the intermediate slopes, c_i 's and c_i^* 's are the corresponding weights given to slopes for the fifth and fourth-order solvers respectively, a_i 's and b_{ij} 's are the coefficients given by Cash & Karp [6]. The error estimate is given by

$$\Delta_1 \equiv u_{n+1} - u_{n+1}^* = \sum_{i=1}^6 (c_i - c_i^*) r_i$$

The coefficients of a_i , b_{ij} , c_i and c_i^* are chosen from Cash & Karp [6] and are given in the table below.

i	a_i			b_{ij}			c_i	c_i^*
1 2 3	1 593	1 500	9				$\frac{37}{378}$ 0 $\frac{250}{691}$	$ \begin{array}{r} \hline 2825 \\ \hline 27648 \\ 0 \\ \hline $
4 5 6	$ \begin{array}{r} \overline{10} \\ \overline{3} \\ \overline{5} \\ \overline{1} \\ \overline{7} \\ \overline{8} \end{array} $	$ \begin{array}{r} \overline{40} \\ \overline{3} \\ \overline{10} \\ \underline{-11} \\ \overline{54} \\ \underline{1631} \\ \overline{55296} \end{array} $	$ \begin{array}{r} \hline 40 \\ -9 \\ \hline 10 \\ \hline 5 \\ \hline 2 \\ \hline 512 \\ \end{array} $	$ \begin{array}{r} \frac{6}{5} \\ -70 \\ \hline 27 \\ 575 \\ \hline 13824 \end{array} $	$\begin{array}{r} \frac{35}{27} \\ 44275 \\ \hline 110592 \end{array}$	253 4096	$ \begin{array}{r} 250 \\ 621 \\ 125 \\ 594 \\ 0 \\ 512 \\ 1771 \end{array} $	$ \begin{array}{r} \hline 48384 \\ 13525 \\ \hline 55296 \\ \hline 277 \\ \hline 14336 \\ \hline \frac{1}{4} \end{array} $
	j	1	2	3	4	5	6	•

The step-sizing Δt is controlled by means of an adaptive-time-stepping given by the relation

$$\Delta t_0 = \Delta t_1 \left| \frac{\epsilon_0}{\epsilon_1} \right|^{0.2}$$

where Δt_0 is the desired step-size, Δt_1 is the actual step-size, ϵ_0 is the desired accuracy, and ϵ_1 is the accuracy obtained with a step-sizing of Δt_1 . If the error ϵ_1 does not remain within the user-defined value of ϵ_0 , then a new step-size Δt_0 is chosen by the aforementioned equation.

The Duffing equation (Eqn. 1) is split into two parts as shown below.

$$\dot{u} = v \tag{15a}$$

$$\dot{v} = \Gamma \sin(\omega t) + \frac{L(t)}{mD} + \beta u - \alpha u^3$$
 (15b)

Then values of \dot{u} and \dot{v} at the (n+1)-th time-step are obtained by substituting into Eqn. 10.

The current solver is a partitioned FSI solver that is loosely coupled [5]. In this FSI solver, the lift-force of the n-th time-step is transferred from the aerodynamic solver (DVM) to the structural solver to get the displacements and velocities in the (n+1)-th time-step.

3 Results and discussion

The present study investigates the flow-field and loads generated on an airfoil (simplified wing) due to the structural response of a simplified insect-flight-motor [4] subjected to a harmonic forcing. The type of forcing given by the insect to its flight-motor is unknown and hence, a sinusoidal forcing is

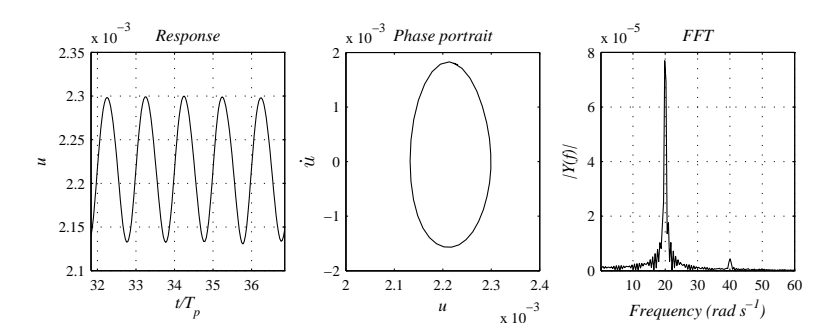


Figure 4: Structural response at $\Gamma = 85$, with phase portrait and FFT

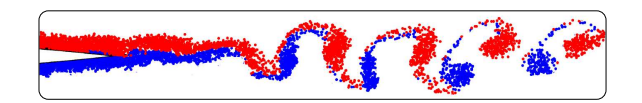


Figure 5: Wake patterns at $\Gamma = 85$

assumed in accordance with Brennan et al. [4]. In the present work, the values of α an β in Eqn. 1 are kept constant and the structural response, flow-field and loads in a sub-resonance regime ($\frac{\omega}{\omega_0} = 0.4$) are explored by varying Γ as a control parameter. The control parameter Γ is varied till no further qualitative changes in the plunge response are observed and the forcing frequency ω is kept constant at 20 rad s^{-1} . Qualitative changes in the structural response observed at $\Gamma = 85, 505, 530$ and 565 are specifically discussed in this work.

At $\Gamma=85$, the structural response shows a single-well potential which is almost single harmonic and has a frequency same as that of the forcing frequency of $20 \ rad \ s^{-1}$. These are presented in the phase portraits and FFT plots in Figure 4. The equivalent kh_m calculated from the structural response is ~ 0.06 (the reduced frequency corresponds to $20 \ rad \ s^{-1}$). At this kh_m , for a rigidly oscillating airfoil, a Kármán type of wake is to be expected. Kármán wake patterns also generate a non-zero amount of drag when averaged over a finite time-scale [16]. In the present case, the corresponding drag-producing von-Kármán wake structures are shown in Figure 5; a mean finite drag of 0.0149 is obtained. The lift-time history is shown in Figure 6 and is also seen to be predominantly single-harmonic with frequency same as the forcing frequency, which can be confirmed from the FFT plots.

As the control parameter Γ is increased, the structural response gradually shows increased influence of higher harmonics. At $\Gamma = 505$, it resembles a

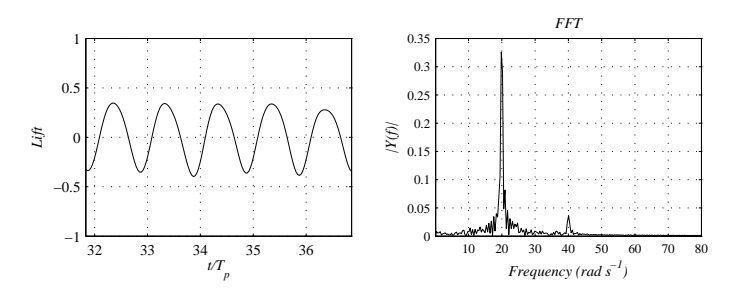


Figure 6: Lift-Time history and corresponding FFT at $\Gamma=85$

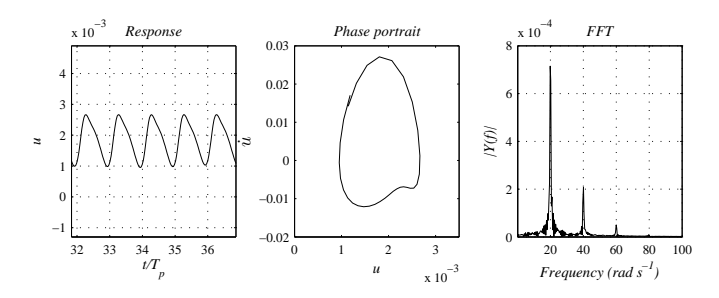


Figure 7: Structural response at $\Gamma = 505$, with phase portrait and FFT

triangular waveform as shown in Figure 7. In the associated phase portrait, one can also see a small kink at the bottom-right corner. The FFT plot of the structural response at $\Gamma=505$ (Figure 7) shows presence of higher harmonics at 40 and 60 $rad~s^{-1}$ in addition to the main peak at 20 $rad~s^{-1}$. The strength of its odd and even multiples at 40 and 60 $rad~s^{-1}$ are small, compared to the fundamental frequency peak at 20 $rad~s^{-1}$, and contributes to imparting a triangular shape to the structural response.

Please note that the structural response resembles a kinematics with a fast upstroke and slow down-stroke. The corresponding flow-field is shown in Figure 8. A single large clockwise vortex is generated in the upstroke $(1R_{ci})$;

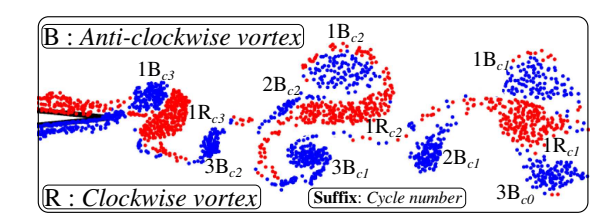


Figure 8: Wake pattern formed at $\Gamma = 505$

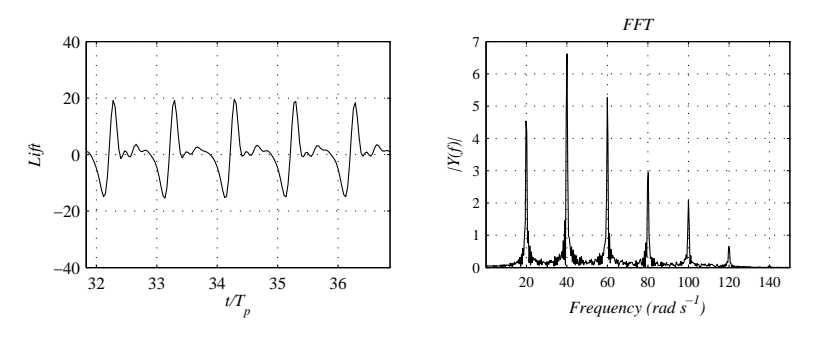


Figure 9: Lift-Time history and corresponding FFT at $\Gamma = 505$

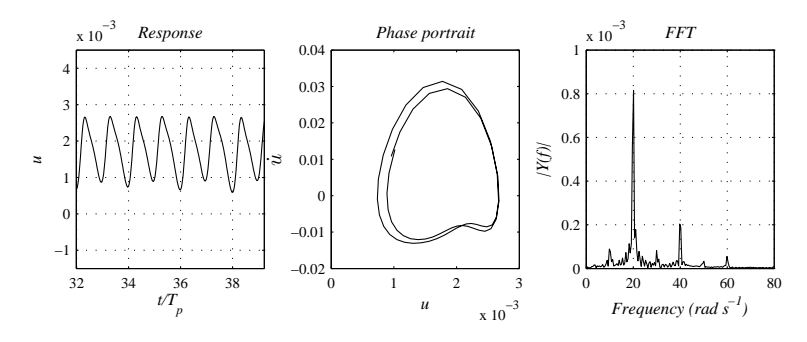


Figure 10: Structural response at $\Gamma = 530$, with phase portrait and FFT

the down-stroke being comparatively slower, generates three smaller anticlockwise vortices from the trailing edge $(1B_{ci}, 2B_{ci} \text{ and } 3B_{ci})$, where $()_{ci}$ denotes the cycle number. The clockwise vortex $1R_{ci}$ pairs with the counterclockwise vortex $1B_{ci}$. The clockwise vortex $1R_{ci}$ then undergoes vortex tearing and pairs with the third anti-clockwise vortex from the previous cycle $3B_{c(i-1)}$ (Figure 8). Hence the final wake pattern from the discussed plunge movement has a vortex pair in the upper row and two anti-clockwise vortices in the lower row (Figure 8), and results in an asymmetric wake pattern. Such wake patterns in plunging airfoils have not been reported so far in the literature.

The lift-response for this case of forcing at $\Gamma=505$ is given in Figure 9. The asymmetry in the wake pattern is reflected in the lift time history as well, as seen in Figure 9. The FFT of the lift-response in Figure 9 shows large number of odd and even harmonics that are multiples of $20 \ rad \ s^{-1}$. It is also interesting to notice that the presence of second and third harmonics are significantly more compared to the previous case. A positive mean thrust of 0.0953 is observed in this case.

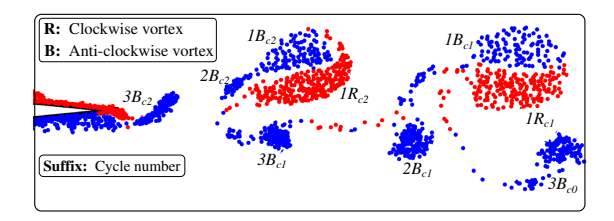


Figure 11: Wake pattern formed at $\Gamma = 530$

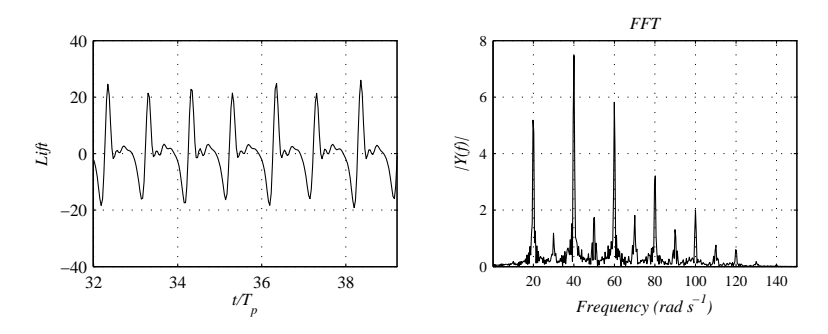


Figure 12: Lift-Time history and corresponding FFT at $\Gamma = 530$

When the forcing amplitude Γ is increased to 530, the structural response shows a period-doubling phenomenon (Figure 10). This is clearly evident from the phase portrait that shows two separate closed loops. The FFT of the structural response shows two small peaks at 10 and 30 $rad\ s^{-1}$, in addition to the forcing frequency and its harmonics. These smaller peaks signify the presence of period doubling in the response. The corresponding flow-field for $\Gamma = 530$ is given in Figure 11. They are not qualitatively very different from the case of $\Gamma = 505$ (Figure 8) as the plunge time histories for both the cases are not qualitatively very different, except the presence of the period doubling. A clockwise vortex is generated during the faster upstroke $(1R_{ci})$ of the kinematics and three anti-clockwise vortices are generated during the relatively slower down-stroke $(1B_{ci}, 2B_{ci} \text{ and } 3B_{ci})$. The clockwise vortex $(1R_{ci})$ then pairs with the first anti-clockwise vortex from the current cycle $(1B_{ci})$ and undergoes vortex tearing, and finally pairs with the third clockwise vortex from the previous cycle $(3B_{c(i-1)})$. This chain of events is very similar to the previous case. All the vorticity cycles look alike and there is no apparent manifestation of period doubling on the wake structure. The lift time history and the FFT for the case of $\Gamma = 530$ is shown in Figure 12 and is very similar to the case of $\Gamma = 505$ presented in Figure 9. However, the FFT behavior of the lift response shows some dif-

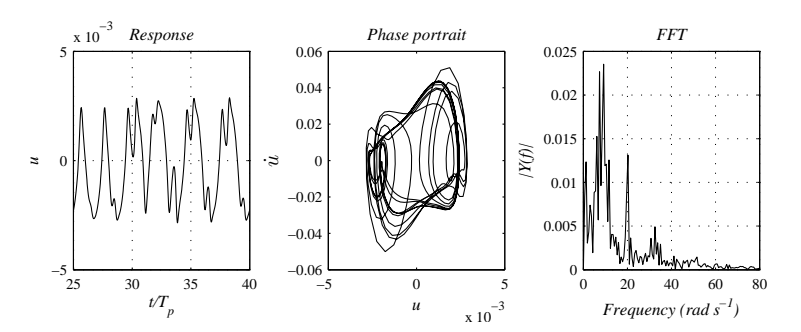


Figure 13: Structural response at $\Gamma = 565$, with phase portrait and FFT

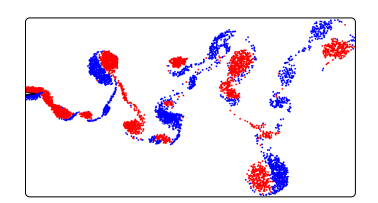


Figure 14: Wake pattern formed at $\Gamma = 565$

ferences. In this case, one can see the not so dominant presence of peaks at the higher harmonics of $10 \ rad \ s^{-1}$. As the structural response amplitude in this case in slightly higher, an increase in the mean thrust is observed which now becomes +0.1238.

Next, Γ is increased to 565 and the structural response is seen to become chaotic and also shows a double-well potential. This is seen from the phase portrait and the FFT plot in Figure 13. The corresponding wake structure is given in Figure 14. There is no identifiable pattern in the wake structures and hence the flow-field can be considered to be chaotic. The lift-time history, along with its FFT, is shown in Figure 15. The lift time-history is also chaotic, and the accompanying FFT plot confirms this by showing a multi-frequency band.

4 Conclusion

A loosely-coupled FSI solver has been developed by coupling a vortex method based Navier-Stokes solver with an embedded Runge-Kutta structural solver. The wake structures and loads generated by the structural response (in plunge direction only) due to a flexible insect-flight-motor has been studied. At low values of forcing amplitude Γ , a single harmonic response is

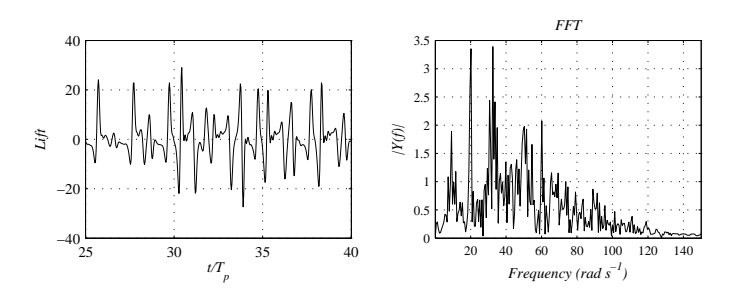


Figure 15: Lift-Time history and corresponding FFT at $\Gamma = 565$

observed. This single harmonic structural response predicts wake structures and loads similar to that of a rigid airfoil in a sinusoidal plunge motion. Further increase in Γ results in multiple frequencies in the structural response which in turn results in unequal speeds of the up and down strokes of the airfoil. This results in an asymmetric flow-field, which is also reflected in the loads. Further increase in Γ shows a period-doubling type of phenomenon. There are no qualitative changes observed in the flow-field as the shape of the structural response is unchanged, except for the period-doubling phenomenon. The aerodynamic load is also qualitatively similar except for the presence of small harmonics at frequencies at half of the forcing frequency. Further increase in forcing amplitude Γ results in a double-well potential with a chaotic structural response. This translates to chaotic wake and aerodynamic loads. Hence, a period-doubling route to chaos has been identified which is characteristic of a forced damped Duffing oscillator.

This study has been conducted at a sub-harmonic regime, where the forcing frequency is dominant. It would of interest to extend this to a resonance regime where the natural frequency of the system becomes dominant.

References

- [1] JM Anderson, K Streitlien, DS Barrett, and MS Triantafyllou. Oscillating foils of high propulsive efficiency. *Journal of Fluid Mechanics*, 360:41–72, 1998.
- [2] G K Batchelor. An introduction to fluid dynamics. Cambridge university press, 2000.
- [3] J Thomas Beale and Andrew Majda. Rates of convergence for viscous splitting of the navier-stokes equations. *Mathematics of Computation*, 37(156):243–259, 1981.

- [4] MJ Brennan, SJ Elliott, P Bonello, and JFV Vincent. The "click" mechanism in dipteran flight: if it exists, then what effect does it have? *Journal of theoretical biology*, 224(2):205–213, 2003.
- [5] M Breuer and M Münsch. Fsi of the turbulent flow around a swiveling flat plate using large-eddy simulation. In *International Workshop on Fluid-Structure Interaction-Theory, Numerics and Applications*, pages 31–43, 2008.
- [6] Jeff R Cash and Alan H Karp. A variable order runge-kutta method for initial value problems with rapidly varying right-hand sides. ACM Transactions on Mathematical Software (TOMS), 16(3):201–222, 1990.
- [7] Alexandre Joel Chorin. Numerical study of slightly viscous flow. *Journal of Fluid Mechanics*, 57(04):785–796, 1973.
- [8] Charbel Farhat, Michel Lesoinne, and Nathan Maman. Mixed explicit/implicit time integration of coupled aeroelastic problems: Three-field formulation, geometric conservation and distributed solution. International Journal for Numerical Methods in Fluids, 21(10):807–835, 1995.
- [9] K. Granlund, B. Monnier, M. Ol, and D. Williams. Airfoil longitudinal gust response in separated vs. attached flows. *Physics of Fluids* (1994-present), 26(2):-, 2014.
- [10] S. Heathcote, Z. Wang, and I. Gursul. Effect of spanwise flexibility on flapping wing propulsion. *Journal of Fluids and Structures*, 24(2):183 – 199, 2008.
- [11] Manoochehr M Koochesfahani. Vortical patterns in the wake of an oscillating airfoil. AIAA journal, 27(9):1200–1205, 1989.
- [12] AW Mackowski and CHK Williamson. Direct measurement of thrust and efficiency of an airfoil undergoing pure pitching. *Journal of Fluid Mechanics*, 765:524–543, 2015.
- [13] Max F Platzer, Kevin D Jones, John Young, and JC S. Lai. Flapping wing aerodynamics: progress and challenges. AIAA journal, 46(9):2136– 2149, 2008.
- [14] William H Press, Saul A Teukolsky, William T Vetterling, and Brian P Flannery. Numerical recipes in C: The art of Scientific Computing. Cambridge University Press, 1992.

- [15] Prabhu Ramachandran. Development and study of a high-resolution two-dimensional random vortex method. PhD thesis, Department of Aerospace Engineering, 2004.
- [16] J. C. S. Lai and MF Platzer. Jet characteristics of a plunging airfoil. *AIAA journal*, 37(12):1529–1537, 1999.
- [17] Sanjay P Sane. The aerodynamics of insect flight. The journal of experimental Biology, 206(23):4191–4208, 2003.
- [18] Sunetra Sarkar, Sandip Chajjed, and Anush Krishnan. Study of asymmetric hovering in flapping flight. European Journal of Mechanics B/Fluids, 37(0):72 89, 2013.
- [19] Sunetra Sarkar and Kartik Venkatraman. Numerical simulation of incompressible viscous flow past a heaving airfoil. *International Journal for Numerical Methods in Fluids*, 51(1):1–29, 2006.
- [20] Kunihiko Taira and Tim Colonius. The immersed boundary method: a projection approach. *Journal of Computational Physics*, 225(2):2118–2137, 2007.
- [21] John Young. Numerical simulation of the unsteady aerodynamics of flapping airfoils. PhD thesis, School of Aerospace, Civil and Mechanical Engineering., 2005.